Machine Learning Insights into Probing TRSB via Asymmetric SQUIDs
Vinke, Wessel

Citation
Vinke, W. (2024). *Machine Learning Insights into Probing TRSB via Asymmetric SQUIDs*.

Machine Learning Insights into Probing TRSB via Asymmetric SQUIDs

Machine Learning Insights into Probing TRSB via Asymmetric SQUIDs

Wessel Vinke

Huygens-Kamerlingh Onnes Laboratory, Leiden University
P.O. Box 9500, 2300 RA Leiden, The Netherlands

July 4, 2024

Abstract

The BCS theory of superconductivity is associated with time reversal symmetry. Some unconventional superconductors have shown time reversal symmetry breaking (TRSB). Scanning SQUIDs may be used to measure features of TRSB. However, probing TRSB using SQUIDs requires sensitivity at zero field, which only asymmetric SQUIDs achieve. Measurements of three SQUIDs asymmetric in arm length, one SQUID asymmetric in arm width and one symmetric SQUID are presented. Furthermore, the parameter values of the SQUIDs are fitted using a neural network that simulates SQUID voltage response.

1

Introduction

The Bardeen-Cooper-Schrieffer (BCS) theory is the first theory that attempts to explain the superconductivity discovered by Kamerlingh Onnes's in 1911. It explains superconductivity phenomena as a microscopic effect due to condensation of so-called Cooper pairs. Bardeen, Cooper and Schrieffer received the Noble prize in Physics for this theory in 1972. One feature of the BCS theory is that the two electrons in a Cooper pair have opposite spin and momentum. This entails that the state of the whole Cooper pair is symmetric under reversal of time (TRS). Superconductors that are well described by BCS theory are named conventional.

Nonetheless, experimental techniques like muon spin rotation (μSR) and the polar Kerr effect have been used to detect time reversal symmetry breaking (TRSB) [1–3]. For example, Mayoh, D. A. et al provide evidence for TRSB in La7Pd3 using ÎŒSR [4]. Figure 1.1 shows increased relaxation below T_c, indicative of internal magnetic fields which are associated with TRSB.

Some superconductors with TRSB also shown 'domain walls' between areas with different orientations of the superconducting order parameter [5]. Consequently, these domain walls exert noticable patterns in the magnetic field of a superconductor. Garcia Campos, P. uses a scanning superconducting quantum interference device (SQUID) microscope to visualise the presence of TRSB in UPt3 [6]. Figure 1.2 shows magnetic field measurements using a SQUID microscope on UPt3, indicating TRSB via the presence of a domain wall (which appears roughly as an s-shape).

Measuring TRSB with SQUIDs requires sensitivity around zero magnetic field. Asymmetries in the inductances of the two SQUID arms (denoted by the asymmetry parameter α_L) and the critical currents of the two junctions (denoted by the asymmetry parameter α_I) can create sensitivity
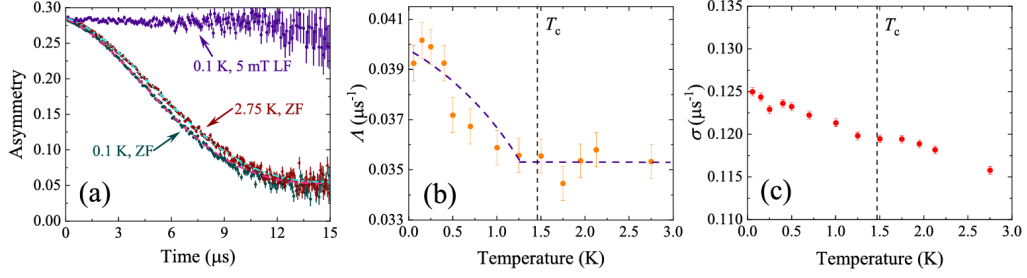
5

Figure 1.1: *(a) ZF and LF-μ SR spectra collected at 0.1 (green) and 2.75 K (red), the data is fit using the Gaussian Kubo-Toyabe model (dashed lines). (b) Temperature dependence of the electronic relaxation rate L can be seen to increase below 1.2 K just below Tc. (c) Temperature dependence of the nuclear relaxation rate Λ shows no change at Tc. Figure and caption from ref. [5].*

at zero field. (The SQUID used for measurements in Figure 1.2 has asymmetric inductance.) In this thesis, I present measurements and analysis of geometrically asymmetric SQUIDs, with the goal of finding out how to create SQUIDs suitable for domain wall measurements of superconductors exhibiting TRSB.

The sensitivity of a SQUID around zero field can be analysed using raw measurement data. Another method of analysis is to fit measured data to simulated data to obtain values for α_L and α_I. Simulating the voltage response of a dc SQUID involves solving a stochastic differential equation. Fitting can therefore be a costly process. Neural networks have shown potential to drastically speed up physics simulations [7]. In that line, I will analyse my data of geometrically asymmetric SQUIDs using neural network simulations.
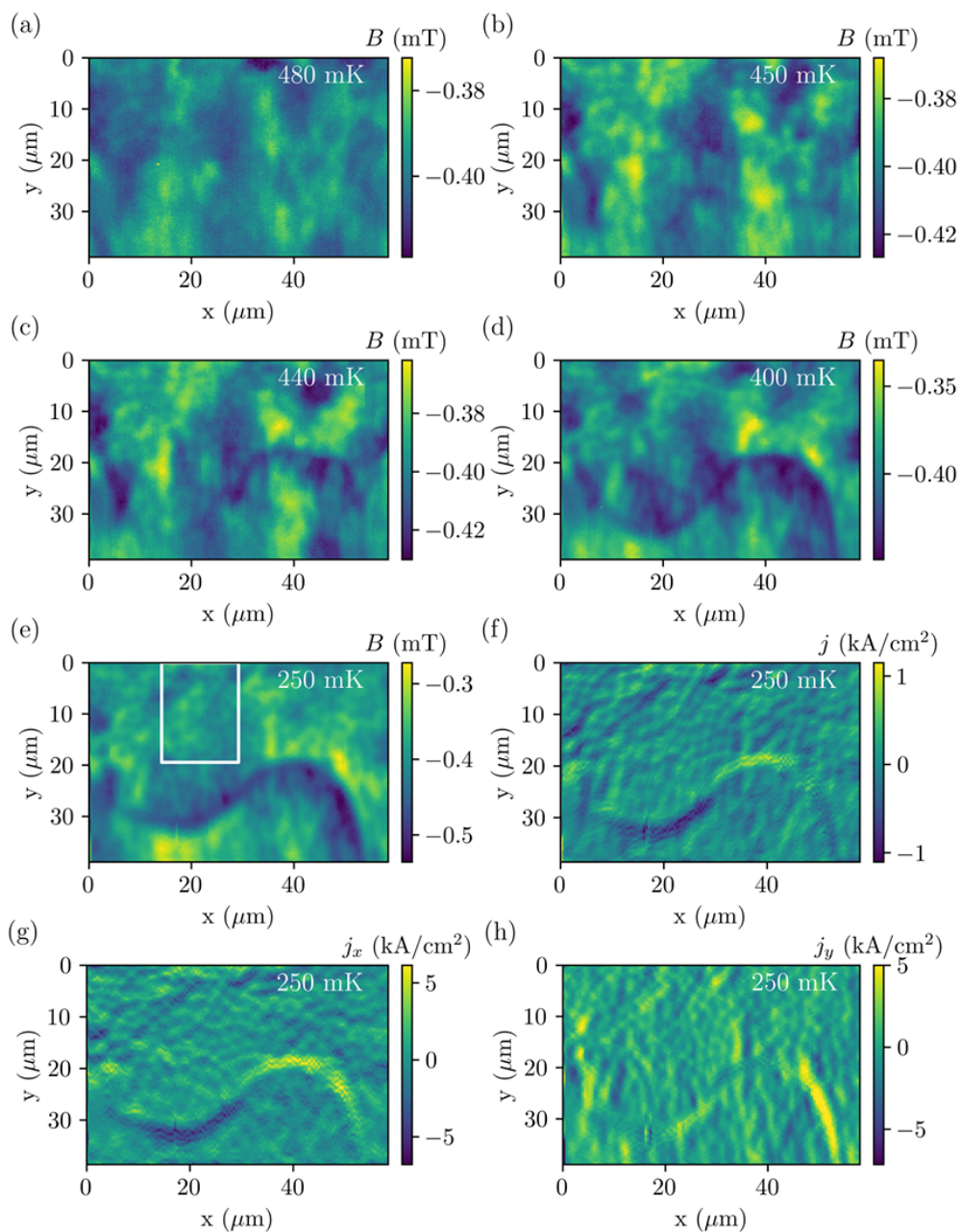
Figure 1.2: *Scans with -400 T applied field before cooling down at a scanning height of 350 nm. The scans were taken decreasing the temperature (from the A-phase to the B phase). Between 450 mK and 440 mK, a sinusoidal domain wall appears, which creates an unusual arrangement of the magnetic flux. At the coldest temperature (250 mK), the mean f ield of the whole scan matches the applied field, and the mean field of one of the two chiral phases (white ROI). Figure and caption from ref. [6].*

Chapter 2

Theory

2.1 London equations & penetration depth

A fundamental feature of superconductivity is the Meissner effect, where a superconductor expels all magnetic fields inside the superconductor. The London equations provide an explanation of the decay of external magnetic fields inside of superconductors [8].

The first London equation is

$$\frac{\partial j_s}{\partial t} = \frac{n_s e}{m_e} E \tag{2.1}$$

Followed by the second London equation:

$$\nabla \times j_s + \frac{n_s e^2}{m} B = 0 \tag{2.2}$$

This ultimately leads to

$$\nabla^2 B = \frac{1}{\lambda_L^2} B \tag{2.3}$$

with the London penetration depth $\lambda_L = \sqrt{\frac{m_e}{\mu_0 n_s e^2}}$. This means that external magnetic fields in superconductors decay exponentially.

2.2 The Josephson effect

A Josephson junction consists of two superconducting electrodes with a weak link connecting them [9]. The type of weak link determines the type

of junction. In the cases of SNS junctions or SIS junctions, the weak link is provided by a normal metal layer or insulating layer respectively. The first Josephson relation provides a one-to-one relation between the supercurrent across two weakly linked superconducting electrodes and the phase different between them for an SIS junction

$$I_s = I_0 sin\delta \tag{2.4}$$

Here I_s denotes the supercurrent across a SIS junction, I_0 the critical current at which voltage becomes non-zero and δ the gauge invariant phase difference. The second Josephson relation relates the voltage U that is developed across the junction to the time derivative of the gauge invariant phase difference $\dot{\delta}$

$$\dot{\delta} = \frac{2\pi}{\Phi_0}U \tag{2.5}$$

Where $\Phi = h/2e$ is the magnetic flux quantum.

The resistively- and capacitively-shunted junction (RCSJ) model of a Josephson junction provides a differential equation relating the phase difference, current and potential difference across the junction. In this model, we apply Kirchhoff's law to the circuit of Figure 2.1 and get:

$$C\dot{U} + \frac{U}{R} + I_0 sin\delta = I + I_N(t) \tag{2.6}$$

where C is the capacitance, R is the resistance, I is the bias current and $I_N(t)$ is the Nyquist noise current. Using the second Josephson relation, we get:

$$\frac{\Phi_0}{2\pi}C\ddot{\delta} + \frac{\Phi_0}{2\pi R}\dot{\delta} = I - I_0 sin\delta \tag{2.7}$$

The current-voltage characteristics of Josephson junctions can show hysteresis: when you go from zero to a current above I_0, $I(V)$ is different than when you go from a current above I_0 to zero. Extermination of hysteresis is usually achieved by using an external shunt resistance in the system with the Josephson junction. This is why the current-voltage characteristics of systems without hysteresis are well explained by the resistively- and capacitively-shunted junction (RCSJ) model.

2.2.1 DC SQUIDs

Direct current superconducting quantum interference devices (dc SQUIDs) are superconducting loops with two arms, where each arm contains a junc-
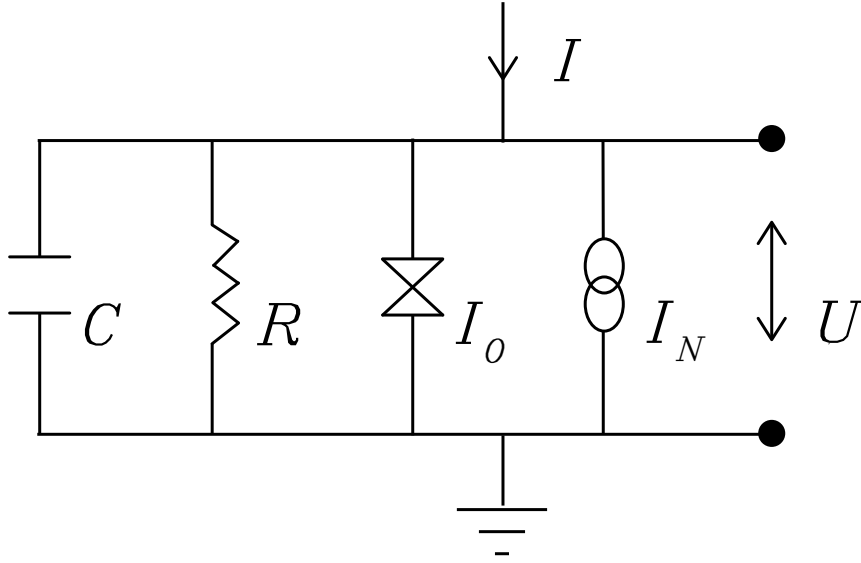
Figure 2.1: *Electrical circuit of the RCSJ model. Starting from the left, the capacitance is located at C, the resistance at E, followed by the Josephson junction with critical current I_0, a Nyquist noise current I_N and lastly a potential difference U.*

tion as shown in Figure 2.2.

The current through each junction is the sum of a contribution from the bias current and a contribution from the circulating current. That is, $I_1 = \frac{I}{2} + J$ and $I_2 = \frac{I}{2} - J$. Combining this with Eq. 2.7 gives us

$$\frac{I}{2} \pm J = I_{0,k} sin\delta_k + \frac{\Phi_0}{2\pi R_k}\dot{\delta}_k + \frac{\Phi_0}{2\pi C_k}\ddot{\delta}_k + I_{N,k} \tag{2.8}$$

with $k = 1, 2$ for the separate junctions.

For any point in the loop visible in Figure 2.2, the wave function must be single-valued. This means that when a path is traversed around the loop from one point to itself, the sum of the phase changes along that path must equal an integer amount of 2π. In the limit of bulk electrodes there are two notable sources of phase change in the dc SQUID: traversing a Josephson junction and traversing a magnetic vector potential. The latter of these effects is commonly accredited to flux, because a closed line integral over the magnetic vector potential is equal to a closed surface integral (Stokes's theorem) over the magnetic field. This in turn can be simplified to a flux quantity Φ.

Following a path around a loop in the dc SQUID, we find that the direction with which the first junction is encountered differs from the second junction. That is, as a path is traversed around the loop, the first junction
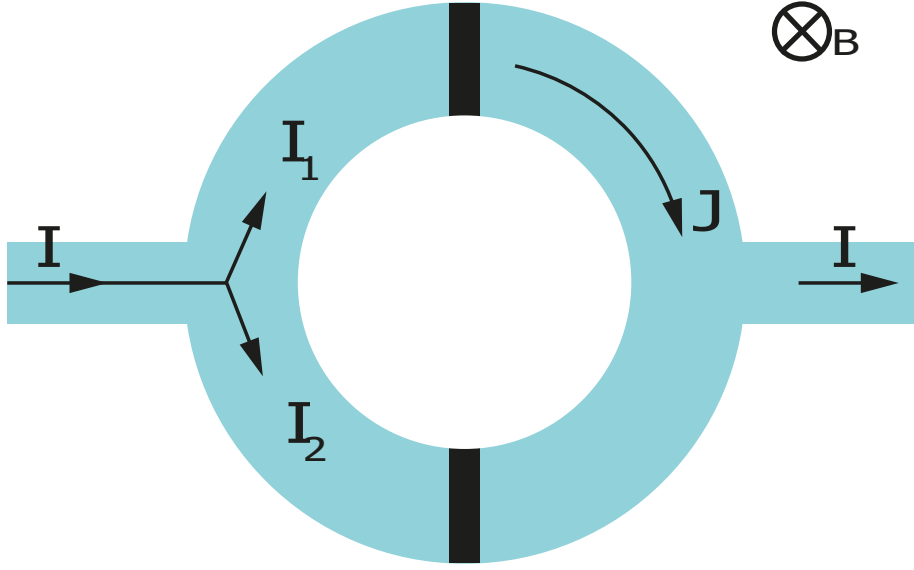
Figure 2.2: *A schematic of the dc SQUID. I represents the external bias current. I_1 and I_2 represent the portions of the bias current going through each arm (and junction). The circulating current induced by the junctions is J. The Josephson juntions are visualised by two black strokes.*

contributes to a phase change of δ_1 while the second junction contributes to a phase change of $-\delta_2$. The phase change due to flux has contributions from both the external magnetic field and the current density J. Then, the single-valuedness of the wave function at any point in the loop requires that

$$\delta_1 - \delta_2 + \frac{2\pi}{\Phi_0}\left(\Phi_a + LJ\right) = 0 \qquad (2.9)$$

with Φ_a being the applied flux, L being the total inductance. This may be rewritten as

$$\delta_2 - \delta_1 = \frac{2\pi}{\Phi_0}\Phi_T \qquad (2.10)$$

with $\Phi_T = \Phi_a + LJ$.

Eq. 2.8 may be normalized using $I_0 = (I_{0,1} + I_{0,2})/2$ for the average critical current, $R = 2R_1R_2/(R_1 + R_2)$ for twice the parallel resistance and $C = (C_1 + C_2)/2$ for the capacitance. Defining the Stewart-McCumber parameter $\beta_c = \frac{2\pi}{\Phi_0}I_0R^2C$ and the screening parameter (also called nor-

malised inductance) $\beta_L = \frac{2LI_0}{\Phi_0}$, we may write Eq. 2.8 in normalised form:

$$\frac{i}{2} \pm j = sin\delta_k + \dot{\delta}_k + \beta_c\ddot{\delta}_k + i_{N,k} \tag{2.11}$$

with $k = 1, 2$ for two junctions and

$$\delta_1 - \delta_2 + 2\pi \left(\phi_a + \frac{1}{2}\beta_L j \right) = 0 \tag{2.12}$$

where $\phi_a = \frac{\Phi_a}{\Phi_0}$.

One last note about the dynamics of (dc) SQUIDs is that the effect of the Nyquist noise term on IV's is characterised by the noise parameter Γ

$$\Gamma = \frac{k_b T}{E_J} = \frac{2\pi k_b T}{\Phi_0 I_0} \tag{2.13}$$

In practice, Γ leads to a rounding of the superconducting transition at the critical current. Figure 2.3 shows how rounding occurs in the voltage-current characteristics of a dc SQUID, which is particularly pronounced at the critical current.

2.2.2 Asymmetry parameters

The two junctions in a dc SQUID may have different critical currents, resistances and capacitances. Furthermore, the different arms of the SQUID to which the junctions are attached may have different inductances. SQUIDs with such differences may be called asymmetric. Asymmetry is modelled by the parameter α. It is defined such that

$$I_{0,1} = I_0(1 - \alpha_I), \quad R_1 = \frac{R}{1 - \alpha_R}, \quad C_1 = C(1 - \alpha_C) \tag{2.14}$$

$$I_{0,2} = I_0(1 + \alpha_I), \quad R_2 = \frac{R}{1 + \alpha_R}, \quad C_2 = C(1 + \alpha_C) \tag{2.15}$$

for the critical currents, resistances and capacitances of the two junctions. Adding these parameters to Eq. 2.11, we get

$$\frac{i}{2} \pm j = (1 \mp \alpha_I)sin\delta_k + (1 \mp \alpha_R)\dot{\delta}_k + \beta_c(1 \mp \alpha_C)\ddot{\delta}_k + i_{N,k} \tag{2.16}$$

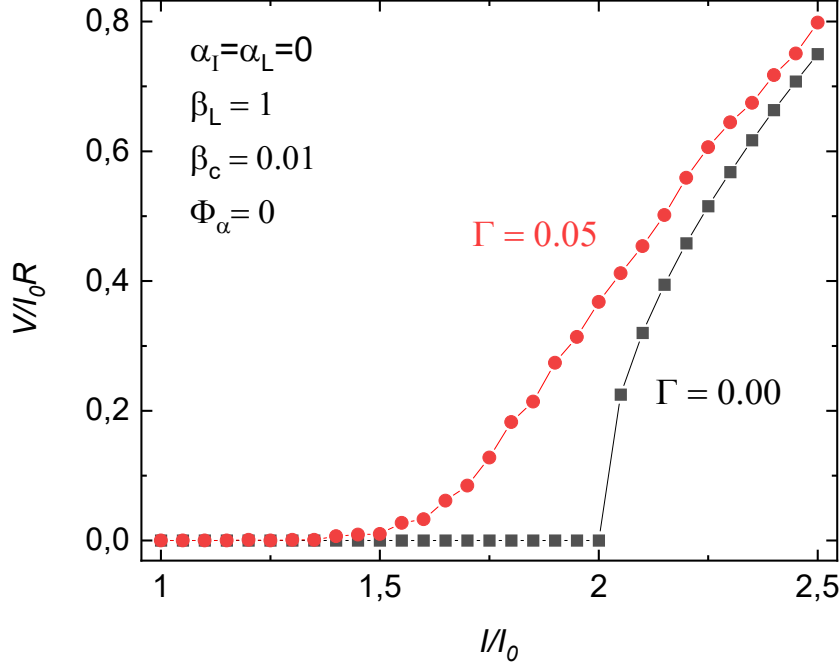Furthermore, for asymmetric arm inductance, Eq. 2.12 changes into:

Figure 2.3: *Simulated normalised voltage-current characteristics of a dc SQUID with two different levels of voltage noise. The red scatter plot has $\Gamma = 0.05$, whereas the black scatter has $\Gamma = 0.00$.*

$$\delta_2 - \delta_1 = 2\pi \left(\phi_a + \frac{1}{2}\beta_L j - \frac{1}{4}\alpha_L \beta_L i \right) = 2\pi\phi_a + \pi\beta_L \left(j - \frac{\alpha_L}{2}i \right), \quad (2.17)$$

These equations should suffice for modelling the dynamics of a dc SQUID with asymmetric critical current, resistance, capacitance and inductance according to the RCSJ model.

Correspondingly, the shift between the maxima of the negative and positive critical current oscillations due to asymmetry is given by [10]:

$$\frac{\Delta\Phi}{\Phi_0} = \beta_L(\alpha_L + \alpha_I) \quad (2.18)$$

Figure 2.4 shows how asymmetry leads to a shift in measured voltages as a function of current and flux.
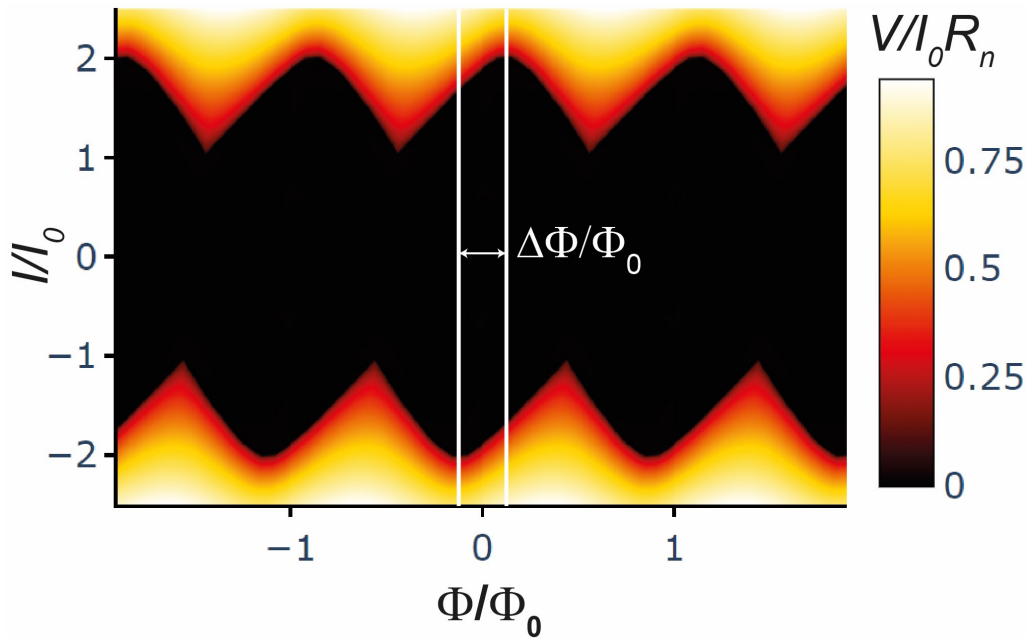
Figure 2.4: *Simulated SQUID interference pattern with $\alpha_L = 0.25$ and $\beta_L = 1$ (with symmetrical critical currents and resistances) operating in the over damped limit ($\beta_c \to 0$). The color transition from black to red points to the critical current. The combination of parameters induces a shift between corresponding peaks in negative and positive critical current oscillations. The shift is $\frac{1}{4}$ normalised flux units.*

3

Design and methods

We are interested in dc SQUIDs that are shifted in this manner as to create a field-sensitive dc SQUID around a magnetic field/flux of zero. I provide a two-component definition of 'field-sensitive' at a given field B_g:

1. There must be some current for which there is a non-zero transfer function $\delta V/\delta B$ at B_g.

2. For such a current the transfer function $\delta V/\delta B$ must behave linearly within a range ρ around B_g, such that ρ is approximately equal to the desired range of field measurements.

If a dc SQUID obeys (1) but not (2), field measurements (through voltage measurements) will fail to measure at the complete desired range of field measurements. Thus, a positive transfer function ($\delta V/\delta B > 0$) at B_g is necessary but insufficient for field-sensitivity at B_g.

Figure 3.1 illustrates how asymmetry induces a shift towards a positive transfer function at zero field (for some dc currents).

3.1 Geometry design and kinetic inductance

For a straight wire of length l with cross section A, the kinetic inductance is given by [11]:

$$L_k = \frac{ml}{nq^2 A} = \frac{\mu_0 \lambda_L^2 l}{A} \tag{3.1}$$

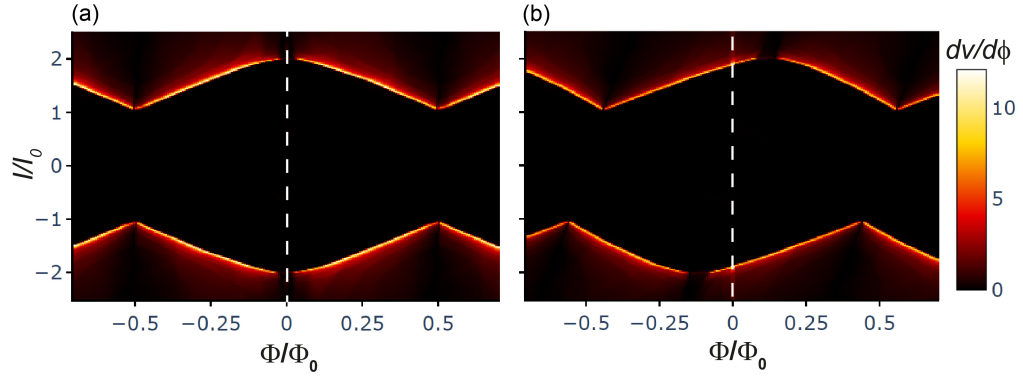With λ_L the London penetration depth from Eq. 2.3.

17

Figure 3.1: *Transfer function $\frac{\delta v}{\delta \phi}$ of the normalised voltage $v = V/I_0 R_n$ as a function of the normalised current i and the normalised flux ϕ with $\Gamma = 0.0$ and $\beta_L = 1.0$. (a) shows the simulated interference pattern for a symmetric SQUID. In (b), $\alpha_L = 0.25$. The white dashed lines are positioned at zero field/flux. For (b), but not for (a), there are currents for which there is a positive transfer function at zero field.*

According to Eq. 2.18, asymmetry in the inductance of the two arms of a dc SQUID induces a shift. For thin films, it may be hypothesized that the kinetic inductance is the main term in the total inductance, and that magnetic inductance is negligible. As Eq. 3.1 shows, the inductance of a wire with an approximately uniform cross section has two geometric components: the length l and the cross section A. In the case of a thin film, the cross section can further be divided into a thickness t and a width w, as to approximate a rectangular cross section. Whereas L_k is proportional to l, it is inversely proportional to t and w. Nonetheless, inductance asymmetry in any of these geometric parameters should theoretically translate to an asymmetry in inductance according to Eq. 3.1.

I therefore attempt to design inductively asymmetric SQUIDs. In thin-film nanofabrication process, the thickness of the film is generally kept constant. Therefore, I design SQUIDs that are asymmetric in the lateral dimensions l and w of each arm of the SQUID. Figure 3.2 shows two sample geometrically asymmetric SQUID designs that are intended to induce a non-zero value for the inductance asymmetry parameter α_L.

3.2   Methods

To test the designs, two SQUIDs devices are made on top of Si/SiO substrates. Before deposition, lithography is used to prepare device patterns
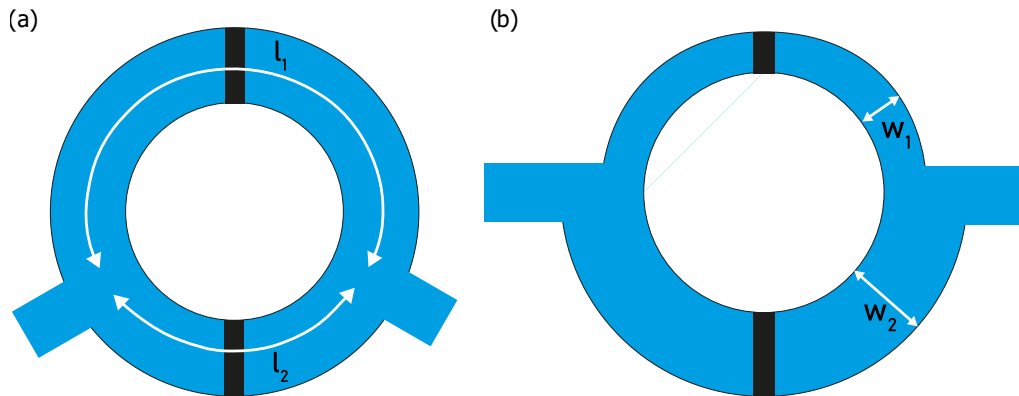
Figure 3.2: *geometrically asymmetric SQUID designs. In (a), the lengths of the two arms are symmetric ($l_1 > l_2$). In (b), the arms lengths are symmetric, but the arm widths are asymmetric ($w_1 < w_2$). If we approximate the loop wire as a straight wire with uniform cross sections, the kinetic inductance will be asymmetric according to Eq. 24.*

that allow wire-bonding of the devices. The used method of deposition is ultra-high vacuum (UHV) sputtering. The first layer deposited is Cu, followed by Nb and lastly Pt. The Cu layer will function as the normal metal layer separating Nb superconducting electrodes. Lastly, Pt has been used as a capping layer, to provide protection for the Nb layer.

After deposition, SQUID patterns are milled out of the metal layers using focused ion beam (FIB) milling. We use a ThermoFisher Aquilos dual beam-FIB, provided by NeCEN [12].

Lastly, the contact pads of the devices containing the SQUIDs are wire-bonded onto the contact pads of the insert puck.

We perform our measurements inside a TeslatronPT cryostat by Oxford Instruments, with a base temperature of 1.5 K. All transport measurements are carried out using standard lock-in techniques with a SynkTek MCL1-540.

Chapter 4

Results

Five SQUIDs have been measured in total. The next sections will show the devices and the measurements.

4.1 Febricated devices

Two chips are fabricated. Chip α has a 20 nm Cu layer on the bottom, stacked by 60 nm Nb and 4 nm Pt. Chip α has a 20 nm Cu layer on the bottom, stacked by 80 nm Nb and 4 nm Pt. Figure 4.1 shows scanning electron microscope (SEM) images of the FIB fabricated SQUIDs for chip α & β. Figure 4.1 shows a total of five SQUIDs: one of which is symmetrically designed (7a), one is designed with asymmetric arm thickness (7c), and three are designed with asymmetric arm lengths (7b, 7d and 7e).

4.2 Resistance versus temperature

Figure 4.2 shows the measured resistances as a function of temperature (RT) for all three SQUIDs from chip α (left plot), and SQUID A from chip β (right plot).

In the left plot, the symmetric SQUID A has a significantly lower resistance above T_c. The critical temperature can be roughly read off by looking at the point where the resistance goes below 10^{-2}. For SQUID αA this is at 3 K, for SQUID αB this is at 2.5 K and for SQUID αC this is at 2.7 K. SQUID βA has a notably higher T_c than all of these at 5 K. This can be attributed to wider arms than those on chip α (see Figure 4.1) and greater thickness.

21

(a)   Chip α SQUID A   (b)   Chip α SQUID B

(c)   Chip α SQUID C   (d)   Chip β SQUID A
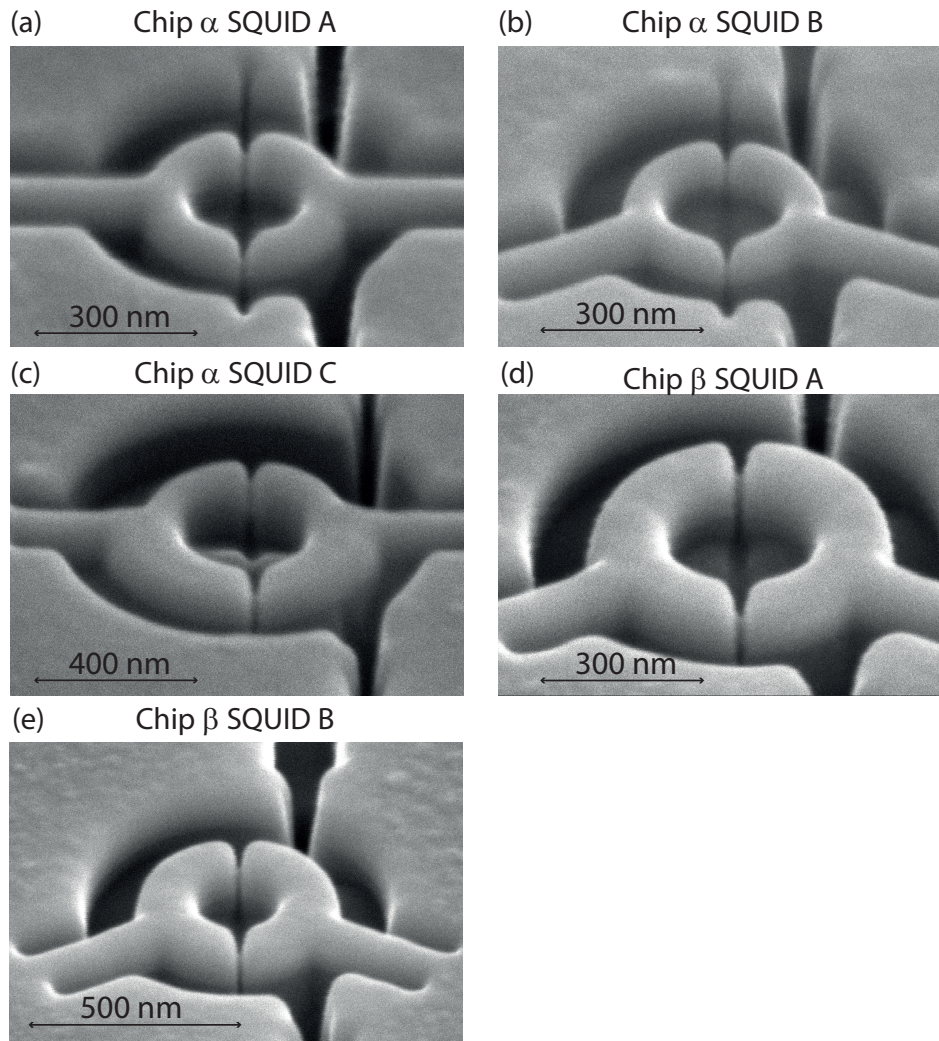

(e)   Chip β SQUID B

Figure 4.1: *SEM images of FIB milled SQUIDs on chip α & β, with SQUIDs named following the Latin alphabet for each chip. (a)-(c) show SQUIDs from chip α, whereas (d) and (e) show SQUIDs from chip β. (b)-(e) are asymmetric: (b), (d) and (e) have asymmetric arm lengths, whereas (c) has asymmetric arm thickness. (a) is symmetric.*

4.3   SQUID interference patterns

SQUID interference (SQI) patterns are measured by taking IV's over a linear space of magnetic fields. Figure 4.3a-e show SQI's for all five SQUIDs presented in this thesis. Figure 4.3a and 4.3b show the same range of magnetic fields, and their I_c oscillations show a similar period. If one looks at
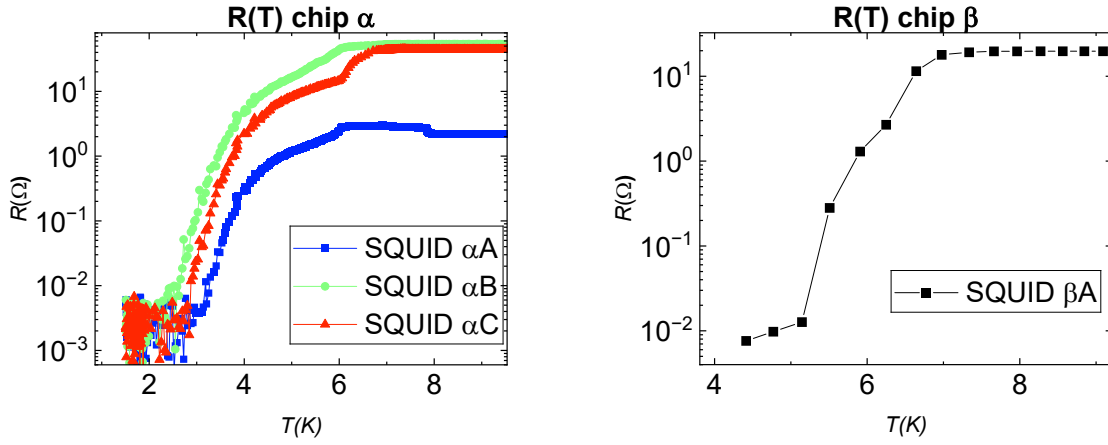
Figure 4.2: *Resistance as a function of temperature for (left) all SQUIDs on chip α, and (right) for SQUID A of chip β.*

Figure 4.3c-e, one notes that there is a red border around the I_c oscillations that has roughly uniform thickness throughout the oscillation. This entails that the voltage increases at roughly the same rate starting at I_c for all magnetic fields. However, for Figure 4.3a-b (showing SQUIDs αA and αB), this is not the case. Simulations show that the uniform 'border thickness' (i.e. rate of voltage increase around I_c) is typical in the RCSJ model (see for example Figure 2.4). As Figure 4.1 shows, the arms of SQUIDs αA and αB have relatively thin arms. This may lead to a superconducting transition in the arms at a current close to I_0, the maximum critical current of the junctions. This would lead SQUIDs αA and αB to less closely resemble the RCSJ model.
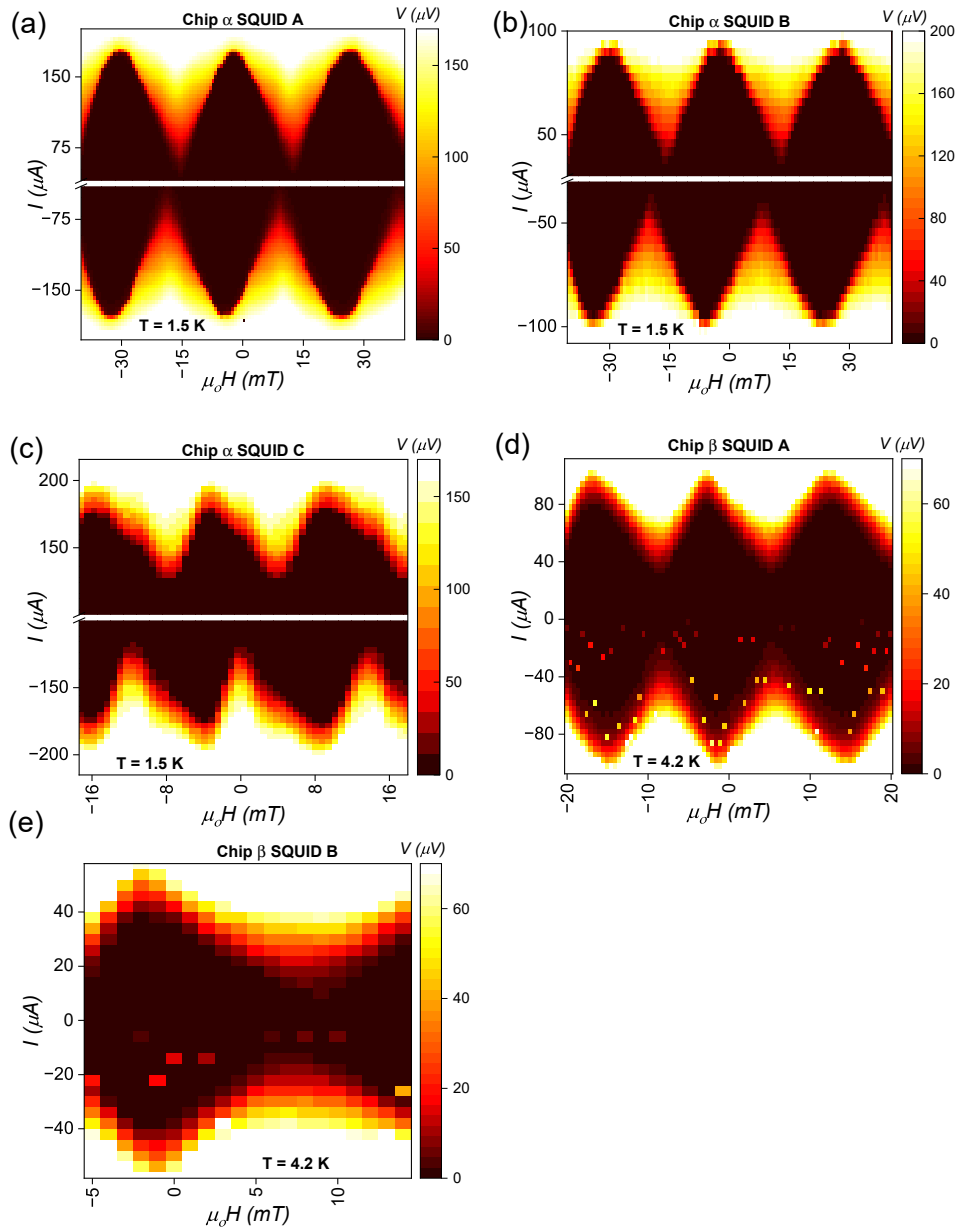
Figure 4.3: *SQUID interference patterns for SQUIDs on chip α & β.*

Chapter 5

Fitting neural network simulations to data

The differential equations provided by the RCSJ model can be simulated to obtain voltages given a set of parameters, currents and fluxes. These simulations can however be temporally costly, requiring over one second to simulate a single voltage. Thus, if one wants to fit measured SQUID data, there is a strenuous contraint on the amount of simulations that one can compare with one's measurements.

Neural networks can speed up this process, because they consist of layers of functions that connect their inputs and outputs, and thereby remove the need to directly solve differential equations. In the next sections, I shall share the training process and architecture of neural networks that I have trained to simulate the RCSJ model, and use it to fit my measured SQUID data.

5.1 Neural network training and architecture

I have trained two neural networks. The first, which I shall name SQUID-net 1.0, is trained on a dataset of simulated voltages, where the parameters α_L, α_I, β_L, β_c and Γ are varied. The second model, which I shall call SQUIDnet 1.1, is trained on a dataset where α_L, α_I, β_L and Γ are varied, as well as the amplitudes of the second to fourth harmonics of the current-phase relations of each junction (separately). The amplitude of the first harmonic is constant at unity, so the total amount of varying higher order harmonic terms is six (three for each of two junctions). β_c is kept constant in the training data of SQUIDnet 1.1, as it came to my attention that sim-

ulated voltages were invariant to changes in β_c in the overdamped limit. Lastly, because of computational constraints, the training data for SQUID-net 1.1 has been created on the ALICE supercomputer.

The SQUIDnet 1.0 model takes α_L, α_I, β_L, β_c, Γ, i and ϕ as inputs. It then consists of five layers of nodes, followed by a predicted voltage output layer of a single node. The activation functions for the five hidden layers are (respectively) ReLu, Sigmoid, ReLu, Sigmoid and lastly ReLu. Each of these layer contains 64 nodes. The mean squared error (MSE) of SQUIDnet 1.0 on a validation dataset (randomised sample of dataset that has not been used for training) was in the order of 10^{-5} $v = \frac{V}{I_0 R_n}$ units.

The SQUIDnet 1.1 model takes α_L, α_I, β_L, Γ, a_{12}, a_{13}, a_{14}, a_{22}, a_{23}, a_{24}, i and ϕ as inputs, where a_{ij} represents the jth sine harmonic of the ith junction. It has five hidden layers with the same activation functions as SQUIDnet 1.0, and also a single voltage prediction output node. Next to difference in input parameters, SQUIDnet 1.1 differs from its predecessor in that each hidden layer contains 256 rather than 64 nodes. This also makes SQUIDnet 1.1 significantly slower at prediction than 1.0. The MSE of SQUIDnet 1.1 on a validation dataset was in the order of 10^{-4} $v = \frac{V}{I_0 R_n}$ units.

5.2   Fits of SQUID data

A gradient descent algorithm has been applied to minimize the mean squared error (MSE) between measured and simulated data. Figures 5.2-5.6 illustrate fits for SQUIDs αC, βA and βB. Estimation of error on parameters has shown tedious if not unachievable. Instead, Figures 5.2-5.6c show histograms of the absolute errors with regards to measured data for each respective fit.

Table 5.1 shows fitted values for α_L, α_I, β_L, Γ, the period, I_0, R_n and the slope of the linear fits in figures 5.2-5.6d (which should approximate R_n when I_{dc} is well over I_0. These parameter values need to be interpreted with the error of the measured data, the neural network and the computational constraints of the gradient descent in mind.

It may be noted that although four out of five SQUIDs are geometrically asymmetric, the biggest absolute value of α_L is 0.1 (for SQUID βA, see table 5.1). Furthermore, the SQUID with asymmetric arm widths has a large α_I of 0.696. One way to explain the unexpectedly low α_L is that the contribution to the total inductance from the geometric inductance is greater than expected. It was hypothesized that kinetic inductance dominates, which is proportional to length. However, our fitted α_L values don't

match the asymmetry in arm length, which should have an α_L of approximately 0.3. At the same time, SQUIDs αB, βA and βB, which are the only SQUIDs with asymmetric arm lengths, also have the highest fitted absolute values for α_L.

Parameter	αA	αB (As. l)	αC (As. w)	βA (As. l)	βB (As. l)
α_L	0.008	0.082	0.002	-0.100	-0.030
α_I	0.096	0.050	0.696	0.013	0.028
β_L	0.862	1.195	0.239	1.32	1.34
Γ	0.009	0.006	0.011	0.035	0.109
Period (mT)	28.7	29.0	13.0	15.6	20.9
I_0 (μA)	86	15	12	52	31
R_n (Ω)	3.12	23.28	24.99	5.39	8.43
a	2.59	17.13	21.44	7.64	4.66

Table 5.1: *Fitted parameters for all five SQUIDs. The variable a refers to the slope of the linear fit in figures 5.2-5.6(d). In the top row, asymmetric SQUIDs have a note with 'As' (followed by l or w, denoting asymmetry in either arm length or arm width respectively). Figure 5.1 (below) shows SEM images of the SQUIDs.*
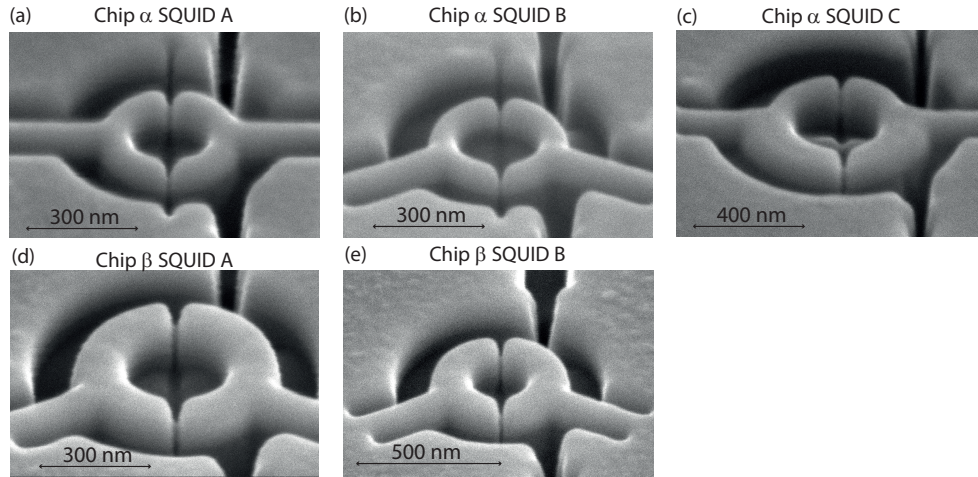

Figure 5.1: *SEM images of FIB milled SQUIDs on chip α & β. (a)-(c) show SQUIDs from chip α, whereas (d) and (e) show SQUIDs from chip β. (b)-(e) are asymmetric: (b), (d) and (e) have asymmetric arm lengths, whereas (c) has asymmetric arm thickness.*
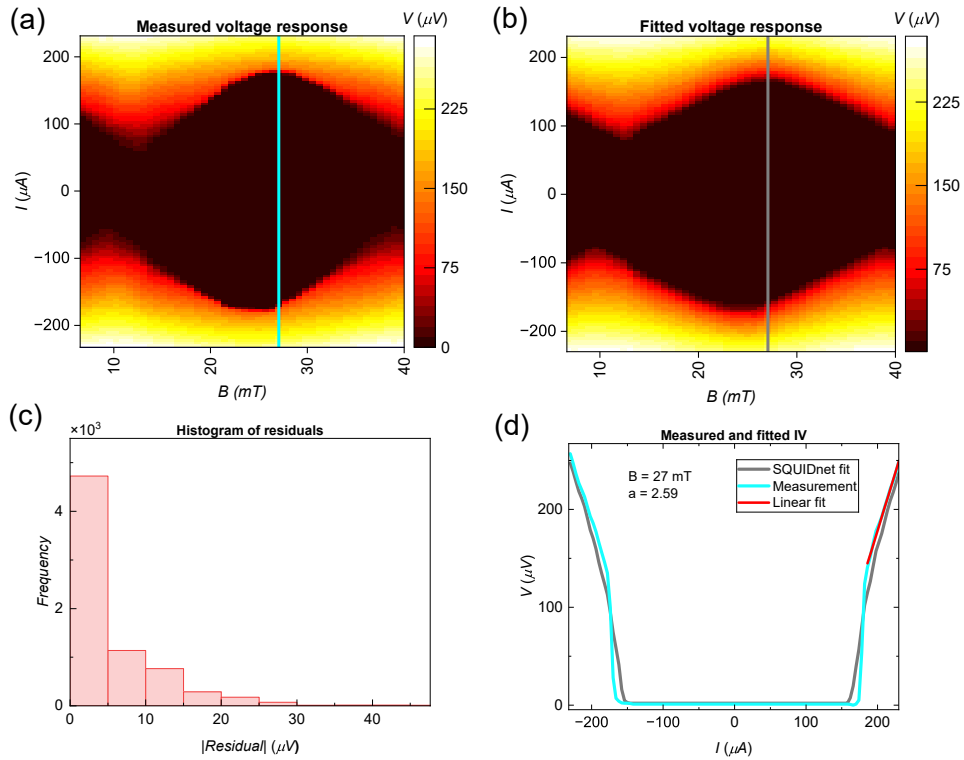
Figure 5.2: *Snippet of measured data (a) for SQUID αA versus fitted data (b) using SQUIDnet 1.0. (c) shows the frequency distribution of the absolute errors between data from (a) and (b) in μV. (d) shows overlap between measurement and fit for a single IV (located in (a) and (b) at vertical lines). (d) also includes a linear fit on the measured IV above I_C, so that its slope a approximates the sheet resistance R_n.*
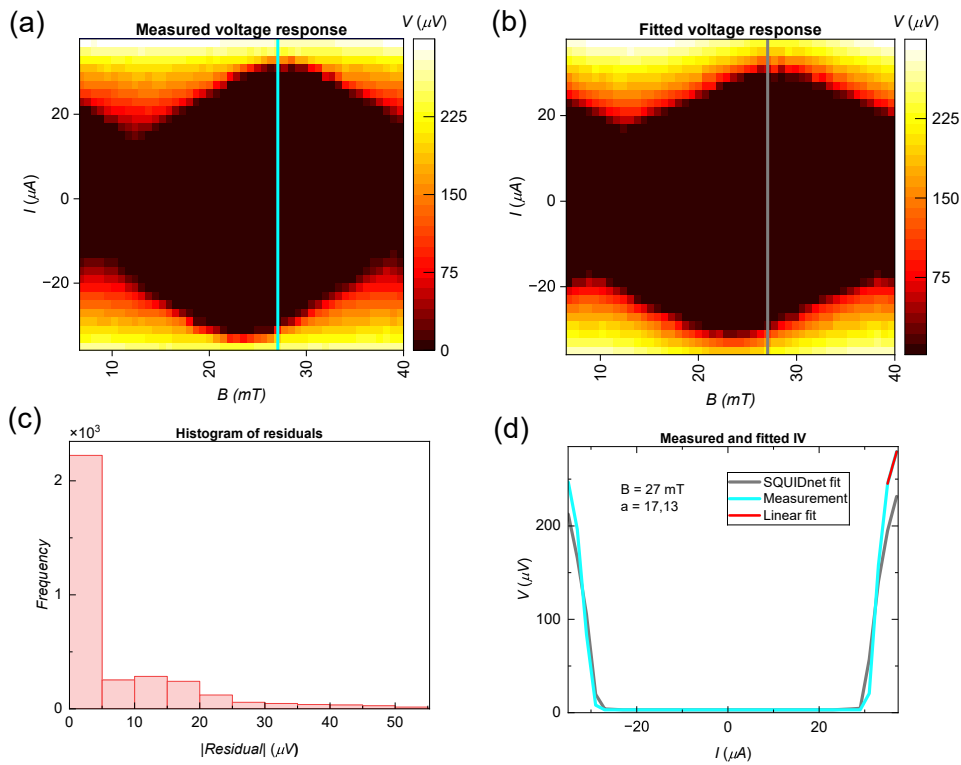
Figure 5.3: *Snippet of measured data (a) for SQUID αB versus fitted data (b) using SQUIDnet 1.0. (c) shows the frequency distribution of the absolute errors between data from (a) and (b) in μV. (d) shows overlap between measurement and fit for a single IV (located in (a) and (b) at vertical lines). (d) also includes a linear fit on the measured IV above I_C, so that its slope a approximates the sheet resistance R_n.*
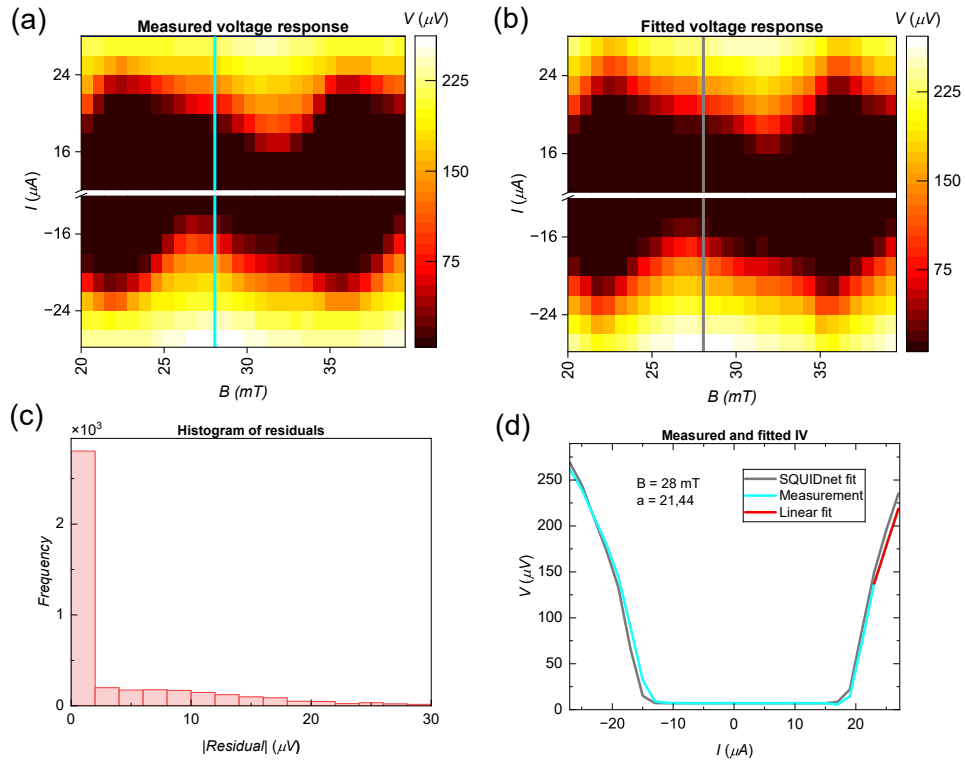
Figure 5.4: *Snippet of measured data (a) for SQUID αC versus fitted data (b) using SQUIDnet 1.1. (c) shows the frequency distribution of the absolute errors between data from (a) and (b) in μV. (d) shows overlap between measurement and fit for a single IV (located in (a) and (b) at vertical lines). (d) also includes a linear fit on the measured IV above I_C, so that its slope a approximates the sheet resistance R_n.*
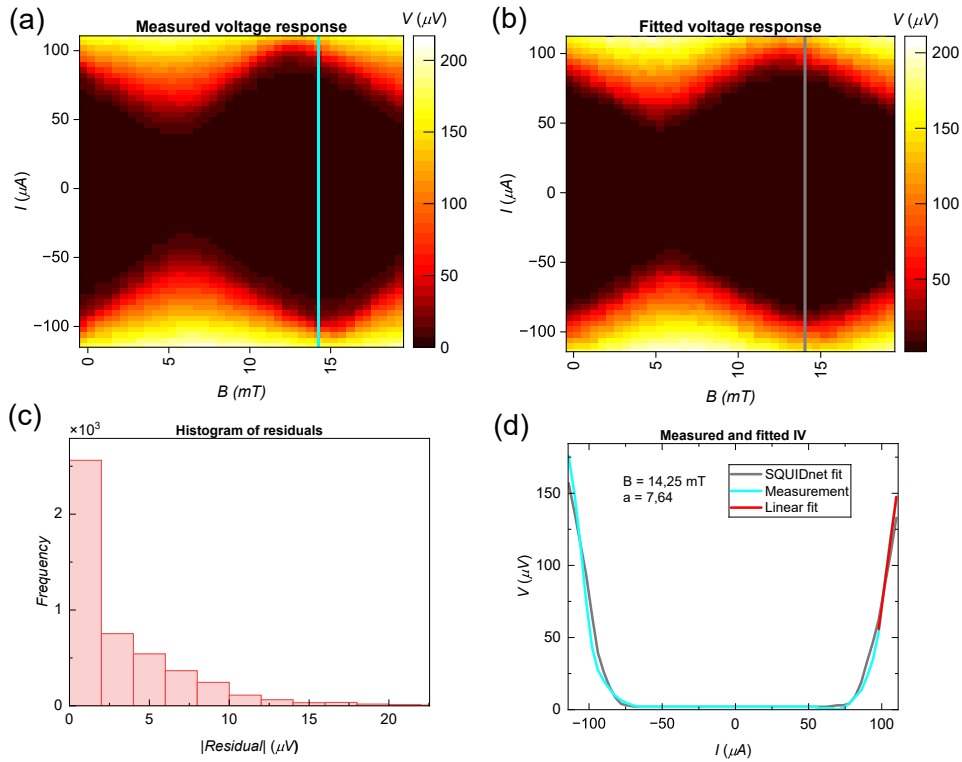
Figure 5.5: *Snippet of measured data (a) for SQUID βA versus fitted data (b) using SQUIDnet 1.0. (c) shows the frequency distribution of the absolute errors between data from (a) and (b) in μV. (d) shows overlap between measurement and fit for a single IV (located in (a) and (b) at vertical lines). (d) also includes a linear fit on the measured IV above I_C, so that its slope a approximates the sheet resistance R_n.*

Figure 5.6: *Snippet of measured data (a) for SQUID βB versus fitted data (b) using SQUIDnet 1.0. (c) shows the frequency distribution of the absolute errors between data from (a) and (b) in μV. (d) shows overlap between measurement and fit for a single IV (located in (a) and (b) at vertical lines). (d) also includes a linear fit on the measured IV above I_C, so that its slope a approximates the sheet resistance R_n.*
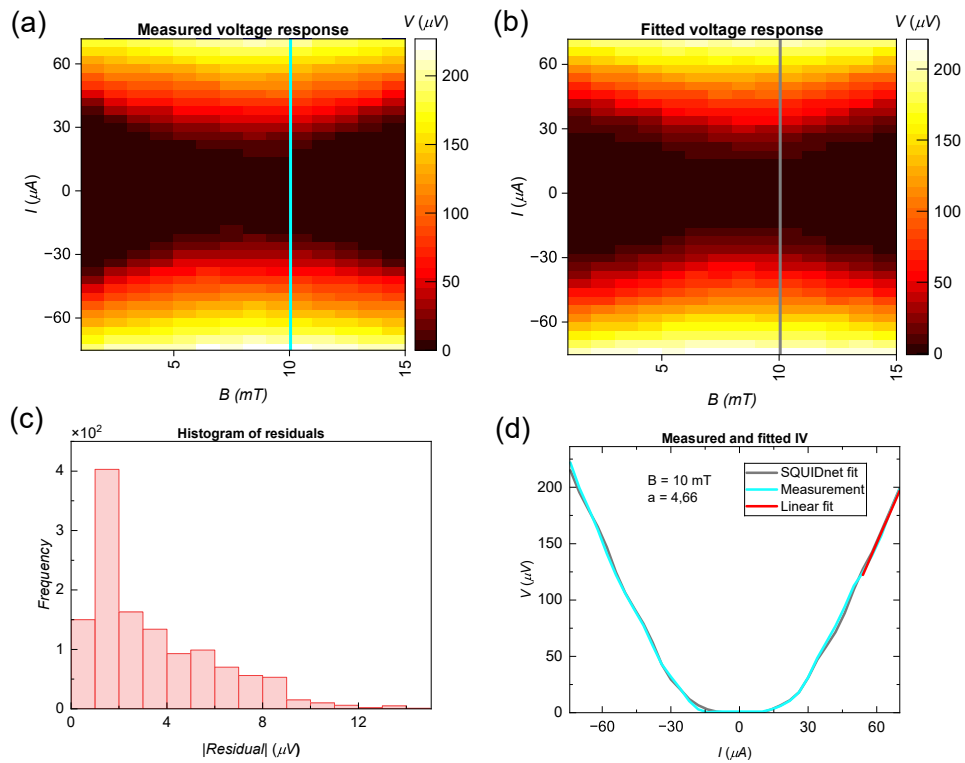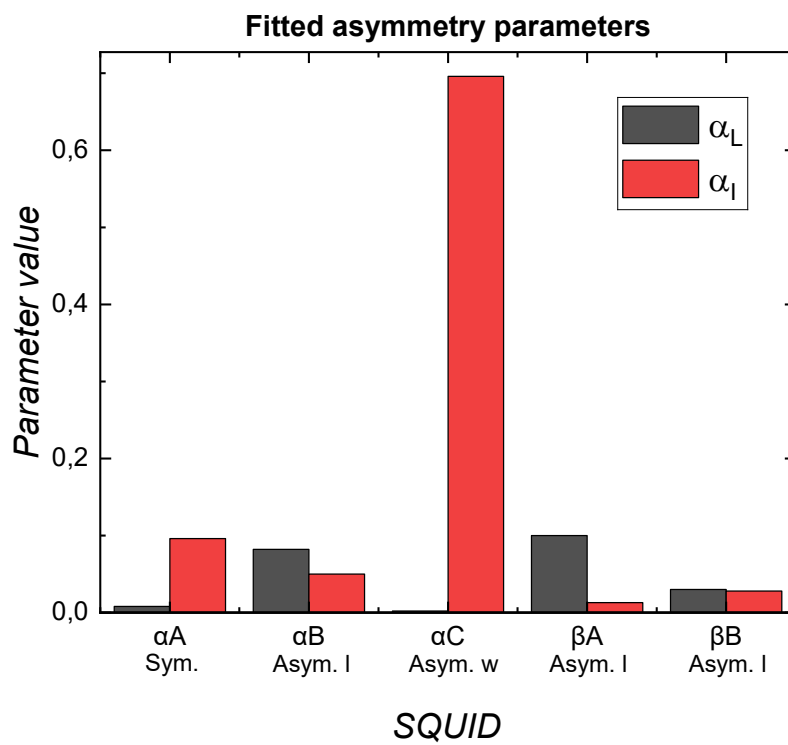
Figure 5.7: *Asymmetry parameters for fits in figures 5.2-5.6. On the horizontal axis, asymmetric SQUIDs have a note with 'Asym' (followed by l or w, denoting asymmetry in either arm length or arm width respectively).*

Chapter 6

Conclusion

It can first be concluded that neural networks are apt to speed up simulations of the RCSJ model. This allows for fitting measured SQUID data within an acceptable time span. SQUIDs have been made by varying the lengths and widths of the SQUID arms. Varying the lengths of the two arms does not change the fitted α_L values as much as one would expect with the hypothesis that kinetic inductance dominates. Still, the SQUIDs with asymmetric arm length did have the highest fitted α_L values. It may be concluded that asymmetric arm length did affect α_L to some extent, but that kinetic inductance does not dominate other effects like geometric inductance. In addition, asymmetric arm width induced a large α_I.

Furthermore, the SQUID with asymmetric arm widths also showed a kink in its critical current oscillation. This is due to the presence of the second harmonic in the current phase relation. It would be interesting to see whether this presence of higher harmonics can be reproduced. If so, this would require a new theoretical explanation for the relation between asymmetric arm or junction width and the presence of higher harmonics. If not, then variation of the arm widths is a highly effective way to make a SQUID suitable for TRSB measurements at zero field, because it creates a large α_I.

Bibliography

[1] B. M. Huddart et al., *Intrinsic Nature of Spontaneous Magnetic Fields in Superconductors with Time-Reversal Symmetry Breaking*, Physical Review Letters **127**, 237002 (2021).

[2] G. Li et al., *Bulk evidence for a time reversal symmetry broken superconducting state in URu2Si2*, (2013).

[3] J. Xia, E. Schemm, G. Deutscher, S. A. Kivelson, D. A. Bonn, W. N. Hardy, R. Liang, W. Siemons, G. Koster, M. M. Fejer, and A. Kapitulnik, *Polar Kerr-effect measurements of the high-temperature YBa2Cu3O6+x superconductor: Evidence for broken symmetry near the pseudogap temperature*, Physical Review Letters **100**, 127002 (2008).

[4] D. A. Mayoh et al., *Evidence for the coexistence of time-reversal symmetry breaking and Bardeen-Cooper-Schrieffer-like superconductivity in La7Pd3*, (2020).

[5] M. Matsamuto and M. Sigrist, *Quasiparticle states near the surface and the domain wall in a $px\hat{A}\pm ipy- wave superconductor$, $Journal of the Physical Society of Japan$ **68**, $994 (1999)$.

[6] P. Garcia Campos, *Visualisation de la supraconductivité chirale en UPt3*, (2021).

[7] F. Rehm et al., *Physics Validation of Novel Convolutional 2D Architectures for Speeding Up High Energy Physics Simulations*, (2021).

[8] F. London and H. London, *The Electromagnetic Equations of the Supraconductor*, Proceedings of the Royal Society A: Mathematical, Physical and Engineering Sciences **149**, 71 (1935).

[9] B. D. Josephson, *Possible New Effects in Superconductive Tunneling*, Physics Letters **1**, 251 (1962).

[10] J. Clarke and A. I. Braginski, *The SQUID Handbook: Fundamentals and Technology of SQUIDs and SQUID Systems*, volume 1, Wiley-VCH, Weinheim, 2006.

[11] A. J. Annunziata, D. F. Santavicca, L. Frunzio, G. Catelani, M. J. Rooks, A. Frydman, and D. E. Prober, *Tunable superconducting nanoinductors*, Nanotechnology **21**, 445202 (2010).

[12] ThermoFisher Scientific, *ThermoFisher Aquilos 2 DualBeam System*, NeCEN (Netherlands Center for Electron Nanoscopy).